

Article

Development of Bubble Characteristics on Chute Spillway Bottom

Ruidi Bai ¹, Chang Liu ¹, Bingyang Feng ¹, Shanjun Liu ¹ and Faxing Zhang ^{1,*}

State Key Laboratory of Hydraulics and Mountain River Engineering, Sichuan University, Chengdu 610065, China; bairuidiscu@163.com (R.B.); sculiuchangvip@163.com (C.L.); 18625801588@163.com (B.F.); drliushanjun@vip.sina.com (S.L.)

* Correspondence: zhfx@scu.edu.cn; Tel.: +86-159-2803-8306

Received: 30 July 2018; Accepted: 23 August 2018; Published: 24 August 2018



Abstract: Chute aerators introduce a large air discharge through air supply ducts to prevent cavitation erosion on spillways. There is not much information on the microcosmic air bubble characteristics near the chute bottom. This study was focused on examining the bottom air-water flow properties by performing a series of model tests that eliminated the upper aeration and illustrated the potential for bubble variation processes on the chute bottom. In comparison with the strong air detrainment in the impact zone, the bottom air bubble frequency decreased slightly. Observations showed that range of probability of the bubble chord length tended to decrease sharply in the impact zone and by a lesser extent in the equilibrium zone. A distinct mechanism to control the bubble size distribution, depending on bubble diameter, was proposed. For bubbles larger than about 1–2 mm, the bubble size distribution followed a $—5/3$ power-law scaling with diameter. Using the relationship between the local dissipation rate and bubble size, the bottom dissipation rate was found to increase along the chute bottom, and the corresponding Hinze scale showed a good agreement with the observations.

Keywords: chute aerator; spillway bottom; air concentration; air bubble frequency; air bubble chord length

1. Introduction

Chute aerators, regarded as a cost-effective method, have been widely used owing to their proven success as a countermeasure in the Grand Coulee dam since 1960 [1]. Previous studies have provided a significant amount of information on the macroscopic air-water flow properties [2–13], such as the air concentration, air entrainment and detrainment. Rutschmann and Hager [2], combining both model and prototype data, proposed two approaches to calculate the air entrainment coefficient $\beta = q_a/q$, where q_a = air discharge and q = water discharge. The air entrainment coefficient was also investigated by, among others, Shi [14], Pinto [15,16], and Low [17]. Chanson [3] investigated the characteristics of chute aerator flow on the distributions of various bubble parameters (void fraction, velocity, air discharge, turbulent diffusivity, etc.) for different inflow Froude numbers. He also provided a better understanding of the air entrainment processes and found a strong detrainment process occurred in the impact zone. Kramer et al. [5] divided the chute aerator into five zones: inflow region; air detrainment region; minimum air concentration region; air entrainment region; and uniform mixture flow region, and systematically investigated the air detrainment gradients in the far-field of chute aerators. Pfister and Hager [6–8] measured the air concentration and divided the chute aerator into three zones: jet zone, reattachment and spray zone, and far-field zone. The authors also discussed the air entrainment and proposed two comprehensive methods to calculate the average and bottom air concentration development using deflectors and offsets along the chute. Avoiding the upper aeration effect, Bai et al. [9] divided the chute aerator into three zones and found that an

intensive air detrainment occurred in the impact zone and the detrained air escaped into the cavity zone. The previous experimental investigations are summarized in Table 1.

Table 1. Experimental investigations of Chute Spillways.

Reference	V_0 (m/s)	h_0 (m)	F_0	Remarks
Chanson [3]	9.2	0.023	19.5	Model ($W = 0.25$ m)
	6.2–11.3	0.035	10.5–19.5	
	5.3	0.081	6.0	
Prifser [6–8]	4.7–7.5	0.041–0.066	7.4–9.3	Model ($W = 0.30$ m)
Bai [9,10]	4.0–9.0	0.15	3.3–7.4	Model ($W = 0.25$ m)
Shi [14]	14.0	0.058	18.6	Model ($W = 0.20$ m)
Pinto [15,16]	19.5–27.7	0.38–1.06	7.1–10.3	Prorotype (Foz do Areia)
	19.9–32.7	0.38–1.43	8.7–11.1	
	19.9–36.2	0.38–1.29	10.3–11.4	
Low [17]	4.2–9.5	0.05	6–13.5	Model ($W = 0.25$ m)

Many studies concerning the minimum or critical air concentration to avoid cavitation erosion have been conducted [18,19]. Peterka [18] found that when the average air concentration was between 0.01 and 0.06, no cavitation erosion was observed. Up to now, there is no reliable design guideline for the distance required between two aerators to produce sufficient bottom air concentration [5]. Based on prototype observations on Russian dams, Semenkova and Lantyaev [20] provided an average bottom air concentration decay of 0.40% to 0.80% per chute meter.

However, air concentration governs the comprehensive performance of the bubbles, including their chord length and frequency form. In particular, Robinson [21], Xu et al. [22], and Brujan [23] adopted advanced techniques to investigate the mechanism of erosion damage and found that the interaction between the air bubbles and cavitation bubbles was the mechanism that assisted in the prevention of erosion damage. These studies indicate that the bubble size and frequency are significant parameters for the mechanism of erosion damage. However, negligible research has been conducted on the spillway bottom air microcosmic characteristics such as the bottom bubble frequency and chord size. Such investigations are difficult because of the complex nature of the flow and strong impaction of the bottom. In the present study, the development of the bottom bubble characteristics was measured and analyzed.

2. Hydraulics Model

The experiments were conducted in a rectangular chute that was 0.25-m wide with a variable bottom slope $5.71^\circ \leq \alpha \leq 18.2^\circ$ (Figure 1). The measured section was 5-m long and consisted of a smooth convergent nozzle with a width of 0.25 m and height of 0.15 m. The approach flow depth was $h_0 = 0.15$ m and the emergence angle was $0^\circ \leq \theta_0 \leq 14.1^\circ$. The water discharge was supplied by a large tank (3.1-m wide, 3.2-m long, and 9.2-m high) and was measured using a rectangular sharp-crested weir with an accuracy of approximately 1%. In order to gain sufficient velocity, the nozzle was located in the bottom of the tank. A range of approach flow velocities was set from 4.0 m/s to 9.0 m/s. Observations indicated that the approach of the flow was stable. Hence, the Froude number F_0 ($V_0/(gh_0)^{0.5}$) was within the range of 3.3 to 7.4 (Table 2), where g was the gravity. x was the streamwise coordinate along the chute bottom, h_s was the offset height, L was the cavity length, and L_m and L_D were the specific lengths [9].

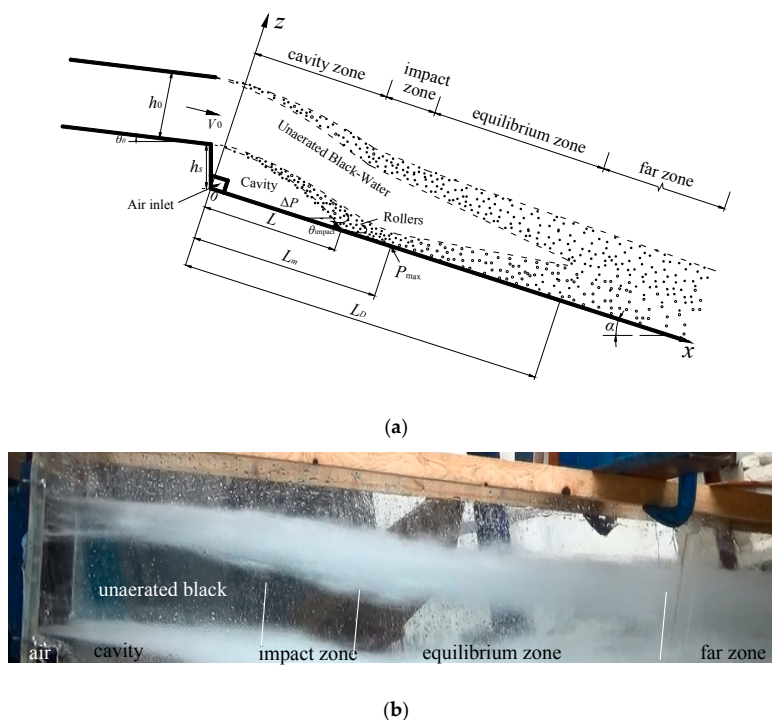


Figure 1. Definition sketch with relevant parameters (a) and side view of chute aerator flow with high speed camera (b).

Table 2. Experimental conditions of chute aerator flow.

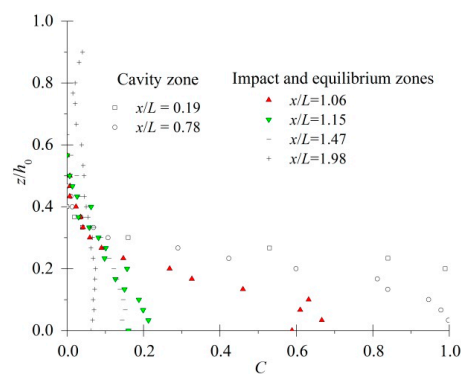
Run	V_0 (m/s)	h_s (m)	θ_0 ($^\circ$)	α ($^\circ$)	F_0
S1	5.0–7.0	0.03	5.71	12.5	3.8–5.8
S2	4.0–6.0	0.05	12.5	18.2	3.3–4.9
S3	5.0–7.0	0.045	0	5.7	3.8–5.8
S4	4.0–6.0	0.045	5.7	14.1	3.3–4.9
S5	6.0–9.0	0.045	14.1	14.1	4.9–7.4

All measurements were performed on the channel centre line. The air-water flow properties were measured with a phase-detection needle probe. The working principle of a conductivity probe was based on the difference in the voltage indices at the platinum tip between the air and water phases. The response time of this sensor was less than 10 μ s. The signals from the conductivity probe were recorded at a scan rate of 100 kHz per for a 40 s scan period. The accuracy of the air concentration was $\Delta C/C = 3\%$, and the bubble frequency was $\Delta f/f = 1\%$, where C was the air concentration and f was the bubble frequency. The length of the impact zone was very short. A few studies in the impact zone have been performed with a space of 0.03 m along the chute bottom.

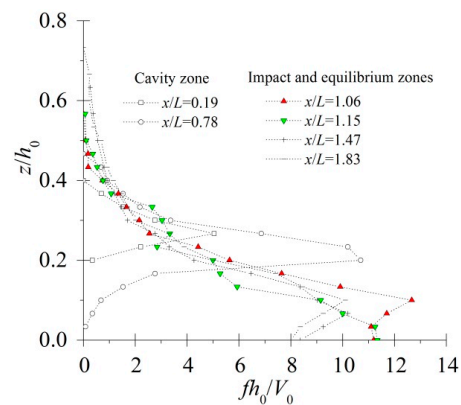
3. Basic Chute Aerator Flow Properties

Air Concentration and Bubble Frequency Profiles

A typical photo of the offset-aerator flow is shown in Figure 2, where four zones were introduced. The typical distributions of the air concentration and bubble frequency in the different zones are depicted in Figure 2 as a function of the dimensionless distance perpendicular to the bottom, i.e., z/h_0 . Owing to a sufficient depth of the approach flow, the unaerated water prevented the upper aeration effect.



(a)



(b)

Figure 2. Distributions of air concentration (a) and bubble frequency (b) along the chute (S5: $V_0 = 9$ m/s, $F_0 = 7.4$).

In the cavity zone ($0 < x/L < 1$), air entrainment occurs in the form of air bubbles entrapped into the lower flow and the air concentration decreased from the lower surface to the vertical direction. At $x/L = 1$, the lower jet impacted on the chute bottom. Further downstream ($x/L > 1$), the distributions of air concentration were different from the cavity zone. Figure 2a shows that the air concentration distributions downstream of the cavity zone, exhibiting an air concentration peak in the turbulent shear region, whereas the air concentration increases from the chute bottom to its maximum value, and then decreases in the vertical direction.

Note that: (1) for $x > L$, the maximum value air concentration C_m decreased sharply in the impact zone, while in the equilibrium zone, the peak air concentration C_m decreased slightly. (2) Experimental results indicated the existence of a maximum value f_m in bubble frequency (Figure 2b), but its location differed from the locus of the maximum void fraction as noticed by Bai et al. [10]. In the cavity, the location of f_m approached $C = 0.50$ with the development of the low jet aeration. The location of f_m was approximately the same as that of the section maximum air concentration C_m at a section in the impact zone, but lower than that in the equilibrium zone.

For more than 25 experiments conducted in this model, only one set of experiments is shown herein to illustrate the basic chute aerator flow property [9]. However, equations presented hereafter are based on all experiments.

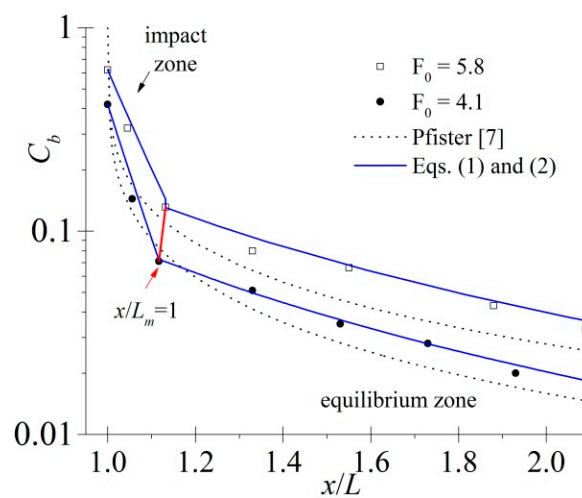
4. Bottom Air Bubble Characteristics

The entrained air from the chute aerator aims to prevent erosion damage. Recent investigations have indicated that the bubble size and frequency are the significant factors preventing erosion damage [22,23]. The air bubbles generated in the cavity zone travelled through the impact zone to

continue downstream. For the chute aerator flows, a large amount of air entrained in the cavity zone was only partially transported to the downstream flow. Under the effect of rollers, large bubbles broke into small bubbles before being transported downstream zone simultaneously in the impact zone.

4.1. Bottom Air Concentration and Bubble Frequency

Bottom air concentration C_b was defined experimentally using the values measured closest to the model chute bottom ($z = 1\text{--}1.5$ mm). The experimental data of bottom air concentration C_b is presented in Figure 3. Note the following: (1) the decay rate of C_b was different in the impact ($L < x < L_m$) and equilibrium zones ($L_m \leq x < L_D$); C_b decreased sharply in the impact zone and decreased slightly in the equilibrium zone. In the impact zone, bottom air concentration $C_b = 0.64$ at $x/L = 1.06$ and it decreased to 0.18 at $x/L = 1.16$. In contrast, the bottom air concentration decreased slightly in the equilibrium zone, with concentration $C_b = 0.145$ at $x/L = 1.31$ decreasing to 0.064 at $x/L = 1.91$. (2) With the increase in F_0 , the values of C_b increase in the present experiments, in agreement with the results of Pfister and Hager [7]. (3) The comparison of the measured values of C_b with the values from the formula proposed by Pfister and Hager [7] is shown in Figure 3, which displays a similar trend downstream of the chute aerator. However, the present values are generally larger than those of Pfister and Hager [7]. At a sufficient water depth, the detrained air bubbles cannot escape into the atmosphere through the upper surface; it can only escape into the cavity zone, which may cause the level of C_b to be larger than that of previous studies. In addition, for a shorter length of the impact zone, the fewer measurement sections may cause an insufficient sharp decrease. (4) It can be concluded that the air transportation regularity is different in the impact and equilibrium zones.



(a)

Figure 3. Cont.

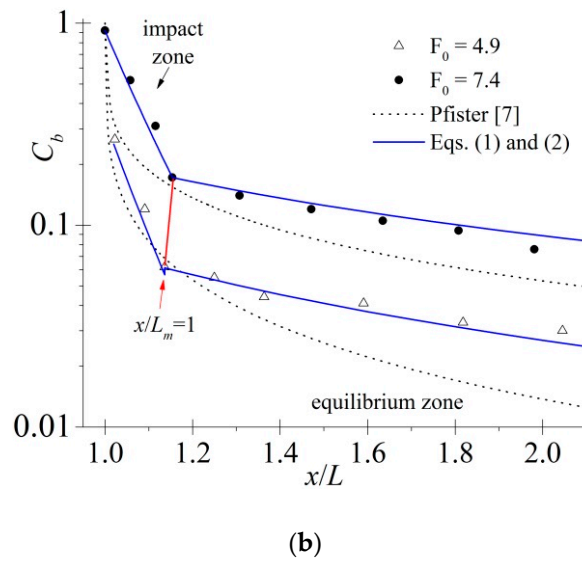


Figure 3. Bottom air concentration along the chute and compared with Pfister [7] (a): S2; (b): S5.

From the experimental data analysis, bottom air concentration C_b can be expressed by the following equation (Figure 3):

$$\frac{C_b}{(C_b)_L} = \left(\frac{x}{L}\right)^{0.985F_0 - 17.5} \quad \text{for } L < x < L_m, R^2 = 0.89 \quad (1)$$

$$\frac{C_b}{(C_b)_{Lm}} = \left(\frac{x}{L_m}\right)^{0.071F_0 - 1.73} \quad \text{for } x > L_m, R^2 = 0.97 \quad (2)$$

where R is the correlation coefficient, $(C_b)_L$ is the bottom air concentration at $x = L$, $(C_b)_{Lm}$ is the bottom air concentration at $x = L_m$.

The experimental data of bottom bubble frequency $f_b h_0 / V_0$ along the chute are displayed in Figure 4. There are a few reports on the chute bottom bubble frequency of the lower jet downstream of the chute aerator. Note the following: (1) $f_b h_0 / V_0$ decreased in both the impact and equilibrium zones, whereas decay rate of $f_b h_0 / V_0$ differed slightly. For $F_0 = 7.4$, $f_b h_0 / V_0 = 11.2$ at $x/L = 1.06$, and it decreased to 10.88 at $x/L = 1.17$ in the impact zone (Figure 4d). In contrast, the bottom bubble frequency decreased slightly more in the equilibrium zone, with $f_b h_0 / V_0 = 9.44$ at $x/L = 1.31$ decreasing to 6.22 at $x/L = 1.91$. (2) In contrast, $f_b h_0 / V_0$ decreased slightly in the impact zone, and there was a large variation in air bubble concentration C_b . (3) Furthermore, $f_b h_0 / V_0$ increased with increasing F_0 .

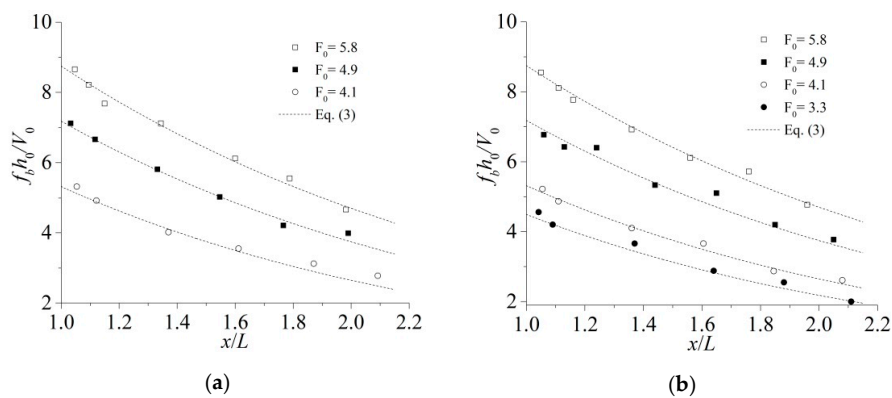


Figure 4. Cont.

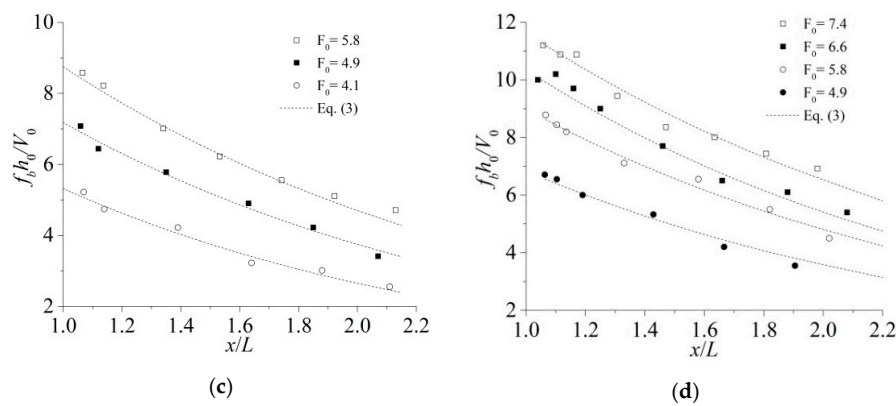


Figure 4. Bottom air bubble frequency along the chute (a): S2; (b): S3; (c): S4; (d): S5.

Overall, the present data could be described by

$$\frac{f_b h_0}{V_0} = 2.81 F_0 \times \exp\left(-\frac{x}{L} F_0^{-0.27}\right) \text{ for } x > L, R^2 = 0.94 \tag{3}$$

where R was the correlation coefficient.

4.2. Bottom Bubble Chord Length Distributions

The chord length distribution of the air bubbles shows microscopic variations passing a measurement point in the stream-wise direction. For all the flow conditions, the experimental results exhibited a broad range of the chord length, varying from less than 0.1 mm to more than 30.0 mm. In this study, the chord length interval was 0.1 mm. The chord lengths are not the bubble diameters, but are the characteristic stream-wise bubble sizes.

Garrett et al. [24] and Deane et al. [25] indicated that the bubble chord length distribution N_a depended on the dissipation rate ϵ and bubble diameter d_{ab} , and the scaling law followed as

$$N_a \propto A \epsilon^{1/3} d_{ab}^{-5/3} \tag{4}$$

where A was a constant, $N_a = N_t/t$, N_t was the number of air bubbles detected in the scan period t ($t = 40$ s).

The distributions of the bottom bubble chord length in the impact and equilibrium zones are depicted in Figure 5. In the impact zone, the air concentration was within the range of $0.10 < C < 0.90$, such that the intermediate region neither corresponded to the high-air concentration region nor to the bubbly flow region. In the equilibrium zone, the maximum air concentration was less than 0.3, so that the zone corresponded to the bubbly flow region. Note the following: (1) the distributions of bottom bubble chord length were skewed with a large proportion of small bubbles. Compared with the impact region, the range of bubble chord length distributions decreased. In the impact zone, the largest probability of bubble chord lengths was concentrated in the range $0.1 \leq d_{ab} \leq 30$ mm, while in the equilibrium zone, the highest probability of bubble chord lengths was concentrated in the range $0.1 \leq d_{ab} \leq 10$ mm. (2) The curve of distribution of the bottom bubble chord sizes was also sharper and narrower along the chute. The power-law scaling of bubble density on diameter is about $\beta = -5/3$ for larger than about 1–2 mm bubbles in the impact and equilibrium zones. (3) In the impact zone, β showed a slight increase from -1.2 at $x/L = 1.06$ to $-5/3$ at $x/L = 1.15$ due to the air detrainment. In the equilibrium zone, β showed a slightly increase from $-5/3$ at $x/L = 1.21$ to -2.4 at $x/L = 1.64$ due to the buoyancy effect.

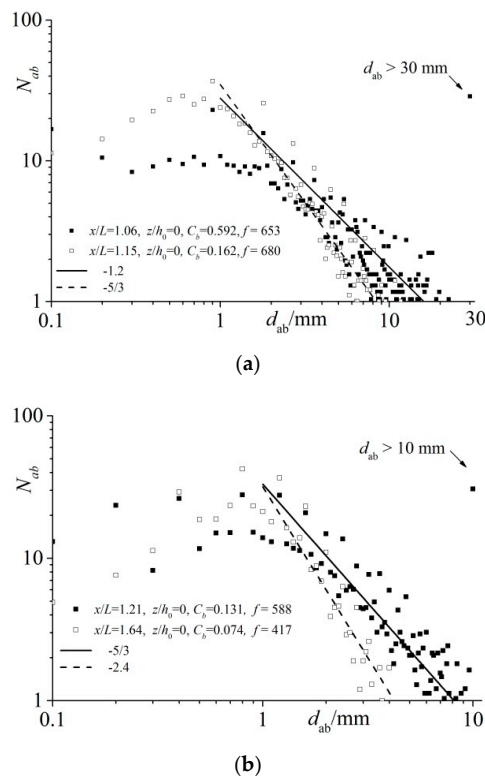


Figure 5. Bottom bubble chord length distributions in the impact zone (a) and equilibrium zone (b) (S5, $V_0 = 8$ m/s, $F_0 = 6.6$).

4.3. Bottom Turbulent Dissipation Rate

Xu et al. [22,23] and Brujan et al. proved that the size of air bubbles near the bottom was a significant parameter for the collapse process of cavitation bubbles. There was little information to investigate the air bubble variations on the chute bottom. The equilibrium zone belonged to the bubbly flow region and the dynamic behavior of the flow was considered to be a steady state air-water two-phase flow.

Hinze [26] indicated that any fluid gas bubbles or droplets were likely to fragment if the pressure forced on its surface exceeds the restoring forces associated with surface tension.

$$\rho \frac{u^2}{\sigma} d_c = W_c \tag{5}$$

where W_c = the critical Weber numbers, u = the turbulent velocity field on the scale of the bubble. If the fluctuating velocity field was assumed to be described by Kolmogorov’s inertial subrange, so that $u^2 = 2\varepsilon^{2/3}d_{ab}^{2/3}$, then only bubbles with diameters larger than the Hinze scale would fragment [17–19].

$$d_c = \left(\frac{W_c \sigma}{2\rho} \right)^{3/5} \varepsilon^{-2/5} \tag{6}$$

where d_c = the Hinze scale, ε = turbulent dissipation rate, which was estimated rather than measured directly. Recent experiments suggest that W_c lied in the range 0.585–4.7, and we have used the value $W_c = 1.0$ (Table 3). For this to exceed a critical value, W_c required that $d > d_c$.

Table 3. Critical Weber numbers for the splitting of air bubbles in water flows.

Reference	W_c	Fluid	Flow Situation	Comments
Hinze [26]	0.585		Two co-axial cylinders, the inner one rotating	Dimensional analysis.
Killen [27]	1.017	Air bubbles in water	Turbulent boundary layer	Experimental data. V in the range 3.66 to 18.3 m/s.
Lewis and Davidson [28]	2.35	Air and Helium bubbles in water and Fluorisol	Circular jet	Experimental data. V in the range 0.9 to 2.2 m/s.
Evans et al. [29]	0.60	Air bubbles in water	Confined plunging water jet	Experimental data. V in the range 7.8 to 15 m/s.
Chanson [3]	1.00	Air bubbles in water	Self-aerated flow	Experimental data. V in the range 3.2 to 5.3m/s.
Martínez-Bazán et al. [30,31]	1.00	Air bubbles in water	Submerged water jet	Experimental data. $V = 17.0$ m/s.
Deane and Stokes [25]	4.7	Air bubbles in water	Breaking waves	Experimental data.
Bai et al. [9]	1.00	Air bubbles in water	Chute aerator flow	Experimental data. V in the range 4.0 to 9.0 m/s.

If the Hinze scale was known, the turbulent energy dissipation rate ϵ on the chute bottom could be estimated from Equation (7). Hinze [26] used the definition that 95% of the air is contained in bubbles with a diameter less than d_c and the calculated turbulent energy dissipation rate ϵ for Deane’s [18] data was much smaller. Garrett et al. [24] used the results of Martínez-Bazán et al. [30,31] and established a one-to-one relationship between the local dissipation rate and bubble size.

$$\epsilon = (1/2)^{5/2} \left(\frac{\sigma}{\rho}\right)^{3/2} \int_0^\infty \left(\frac{d_{ab}}{2}\right)^{1/2} N_a dd_{ab} / \int_0^\infty \left(\frac{d_{ab}}{2}\right)^3 N_a dd_{ab} \tag{7}$$

The bottom dissipation rate ϵ calculated from Equation (7) is shown in Figure 6 and tends to increase in the measured distance. From Equation (6), a change in dissipation rate ϵ from 0.10 to 0.75 $\text{m}^2 \text{s}^{-3}$ corresponded to a change in Hinze scale from 5.5 to 2.4 mm. Thus, the estimate of 2.4 mm for the Hinze scale was in good agreement with the observed change in power-law scaling of the bubble distribution at around 1–2 mm (Figure 5b). Because bubbles smaller than the Hinze scale are stabilized by surface tension forces, a reasonable estimate for this scale is the diameter of the smallest bubbles observed to fragment. In the present study, the bubble chord lengths were smaller than the bubble diameters, due to the measurement technique utilizing conductivity probes. A challenge remains to observe the bubble diameter in a model facility, or even a prototype facility.

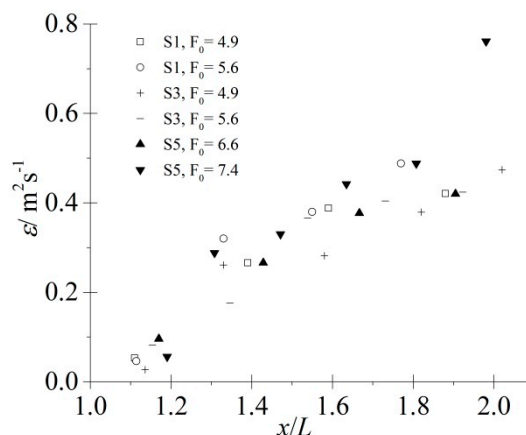


Figure 6. Calculated values of turbulent energy dissipation rate ϵ on the chute bottom.

5. Conclusions

This study presented new information on the bottom air bubble characteristics in the downstream of chute offset-aerators, which were measured with an accurate measurement technique utilizing conductivity probes. For eliminating the upper aeration, the bottom concentration, bubble frequency, bubble chord length, and bottom dissipation rate were analyzed along the chute longitudinal direction. The present study complemented the existing studies on the bubble properties of chute aerator flows.

The bottom air concentration was found to decrease sharply in the impact zone and to decrease slightly in the equilibrium zone. The bottom air bubble frequency was found to decrease slightly along the chute bottom. A formula to predict the bottom bubble frequency in the impact and equilibrium zones was proposed.

Observations showed that the range of probability of bottom bubble chord lengths tended to decrease sharply in the impact zone and to a lesser extent in the equilibrium zone. The bubbles larger than the Hinze scale were subject to fragmentation and showed $-5/3$ power-law scaling with diameter. Using the relationship between the local dissipation rate and bubble size [24], the bottom dissipation rate was found to increase along the chute bottom. The Hinze scale estimated from Equation (6) showed a good agreement with the observed change in power-law scaling of the bubble distribution.

Author Contributions: Conceptualization, R.B., F.Z. and S.L.; Methodology, R.B. and F.Z.; Software, C.L.; Validation, R.B.; Formal Analysis, R.B. and F.Z.; Investigation, R.B.; Resources, S.L.; D.C., B.F.; Writing-Original Draft Preparation, R.B.; Writing-Review & Editing, R.B.; Visualization, B.F.; Supervision, F.Z.; Project Administration, R.B., F.Z. and S.L.; Funding Acquisition, R.B., F.Z. and S.L.

Funding: This work was supported by the National Natural Science Foundation of China (Grant No. 51709293 and Grant No. 51679157), the Fundamental Research Funds for the Central Universities (Grant No. 20826041A4305), and the National Key Research and Development Program (Grant No. 2016YFC0401707).

Conflicts of Interest: The authors declare no conflict of interest.

References

- Pan, S.; Shao, Y. Scale effects in modeling air demand by a ramp slot. *Scale Eff. Model. Hydraul. Struct.* **1984**, *4*, 1–5.
- Rutschmann, P.; Hager, H.W. Air entrainment by spillway aerators. *J. Hydraul. Eng.* **1990**, *116*, 765–782. [[CrossRef](#)]
- Chanson, H. Air bubble entrainment in turbulent water jets discharging into the atmosphere. *Aust. Civ. Eng. Trans.* **1996**, *39*, 39–48.
- Kramer, K.; Hager, W.H. Air transport in chute flows. *Int. J. Multiph. Flow* **2005**, *31*, 1181–1197. [[CrossRef](#)]
- Kramer, K.; Hager, W.H.; Minor, H.-E. Development of air concentration on chute spillways. *J. Hydraul. Eng.* **2006**, *132*, 908–915. [[CrossRef](#)]
- Pfister, M.; Hager, W.H. Chute aerators I: Air transport characteristics. *J. Hydraul. Eng.* **2010**, *136*, 352–359. [[CrossRef](#)]
- Pfister, M.; Hager, W.H. Chute aerators II: Hydraulic design. *J. Hydraul. Eng.* **2010**, *136*, 360–367. [[CrossRef](#)]
- Pfister, M.; Hager, W.H. Chute aerators: pre aerated approach flow. *J. Hydraul. Eng.* **2011**, *137*, 1452–1461. [[CrossRef](#)]
- Bai, R.; Zhang, F.; Liu, S.; Wang, W. Air concentration and bubble characteristics sownstream of a chute aerator. *Int. J. Multiph. Flow* **2016**, *87*, 156–166. [[CrossRef](#)]
- Bai, R.; Liu, S.; Tian, Z.; Wang, W.; Zhang, F. Experimental investigations on air-water flow properties of offse-aerator. *J. Hydraul. Eng.* **2018**, *144*, 04017059. [[CrossRef](#)]
- Li, S.; Zhang, J.M.; Xu, W.L.; Chen, J.G.; Peng, Y. Evolution of pressure and cavitation on side walls affected by lateral divergence angle and opening of radial gate. *J. Hydraul. Eng.* **2016**, *142*, 05016003. [[CrossRef](#)]
- Bai, Z.L.; Peng, Y.; Zhang, J.M. Three-dimensional turbulence simulation of flow in a V-shaped stepped spillway. *J. Hydraul. Eng.* **2017**, *143*, 06017011. [[CrossRef](#)]
- Zhang, J.M.; Chen, J.G.; Wang, Y.R. Experimental study on time-averaged pressures in stepped spillway. *J. Hydraul. Res.* **2012**, *50*, 236–240. [[CrossRef](#)]

14. Shi, Q.; Pan, S.; Shao, Y.; Yuan, X. Experimental investigation of flow aeration to prevent cavitation erosion by a deflector. *J. Hydraul. Eng.* **1983**, *3*, 1–13.
15. Pinto, N.L.S.; Neidert, S.H.; Ota, J.J. Aeration at high velocity flows—Part one. *Int. Water Power Dam Constr.* **1982**, *34*, 34–38.
16. Pinto, N.L.S.; Neidert, S.H.; Ota, J.J. Aeration at high velocity flows—Part two. *Int. Water Power Dam Constr.* **1982**, *34*, 42–44.
17. Low, H.S. Model Studies of Clyde Dam Spillway Aerators. Ph.D. Thesis, University of Canterbury, Christchurch, New Zealand, 1986.
18. Peterka, A.J. The effect of entrained air on cavitation pitting. In *Proceedings of the Minnesota International Hydraulic Convention*; ASCE: Reston, VA, USA, 1953; pp. 507–518.
19. Russell, S.O.; Sheenan, G.J. Effect of entrained air on cavitation damage. *Can. J. Civ. Eng.* **1974**, *1*, 97–107. [[CrossRef](#)]
20. Semenov, V.M.; Lentyaev, L.D. Spillway with nappe aeration. *Hydrotech. Constr.* **1973**, *7*, 437–441. [[CrossRef](#)]
21. Robinson, P.B.; Blake, J.R.; Kodama, T.; Shima, A.; Tomita, Y. Interaction of cavitation bubbles with a free surface. *J. Appl. Phys.* **2001**, *89*, 8225–8237. [[CrossRef](#)]
22. Xu, W.; Bai, L.; Zhang, F. Interaction of a cavitation bubble and an air bubble with a rigid boundary. *J. Hydrodyn.* **2010**, *22*, 503–512. [[CrossRef](#)]
23. Brujan, E.A.; Matsumoto, Y. Collapse of micrometer-sized cavitation bubbles near a rigid boundary. *Microfluid. Nanofluid.* **2012**, *13*, 957–966. [[CrossRef](#)]
24. Garrett, C.; Li, M.; Farmer, D. The connection between bubble size spectra and energy dissipation rates in the upper ocean. *J. Phys. Oceanogr.* **2000**, *30*, 2163–2171. [[CrossRef](#)]
25. Deane, G.B.; Stokes, M.D. Scale dependence of bubble creation mechanisms in breaking waves. *Nature* **2002**, *418*, 839–844. [[CrossRef](#)] [[PubMed](#)]
26. Hinze, J.O. Fundamentals of the hydrodynamic mechanism of splitting in dispersion processes. *AIChE J.* **1955**, *1*, 289–295. [[CrossRef](#)]
27. Killen, J.M. Maximum stable bubble size and associated noise spectra in a turbulent boundary layer. In *Proceedings of the Cavitation and Polyphase Flow Forum*; ASME: New York, NY, USA, 1982; pp. 1–3.
28. Lewis, D.A.; Davidson, J.F. Bubble Splitting in Shear Flow. *Trans. I. Chem. Eng.* **1982**, *60*, 283–291.
29. Evans, G.M.; Jameson, G.J.; Atkinson, B.W. Prediction of the bubble size generated by a plunging liquid jet bubble column. *Chem. Eng. Sci.* **1992**, *47*, 3265–3272. [[CrossRef](#)]
30. Martínez-Bazán, C.; Montañés, J.L.; Lasheras, J.C. On the break up of an air bubble injected into a fully developed turbulent flow. Part 1. Breakup frequency. *J. Fluid Mech.* **1999**, *401*, 157–182. [[CrossRef](#)]
31. Martínez-Bazán, C.; Montañés, J.L.; Lasheras, J.C. On the break up of an air bubble injected into a fully developed turbulent flow. Part 2. Size PDF of the resulting daughter bubbles. *J. Fluid Mech.* **1999**, *401*, 183–207. [[CrossRef](#)]

